Noname manuscript No.
(will be inserted by the editor)

A CRYSTAL-based parameterization of carbon atom dynamic polarizabilities to compute optical properties of curved carbonaceous nanostructures

Michel Rérat, Jean-Claude Rayez, Balázs Fabián, Michel Devel, and Sylvain Picaud

the date of receipt and acceptance should be inserted later

June 27, 2022

Keywords Ab initio calculation, polarizability, cross section, soot, fullerene

Abstract The radiative forcing of dust particles in Earth atmosphere is still poorly characterized. A better estimation of the absorption cross-section of dust particles in the UV-visible part of the spectrum is thus needed. Among the methods used for this purpose, the Atomic Point Dipole Interaction model has the distinctive advantage of being sensitive to the atomistic geometry of the particle and to the chemical functions it contains. However this requires an adequate parameterization of the atomic polarizabilities for all the atomic species forming the particle, over the UV-visible spectrum. In this paper, we illustrate how new methodological improvements based on quantum chemistry, allow taking into account the curvature of the carbon network in the parametrization of the carbon atomic polarizabilities, using the C_{60} molecule to fit the adequate set of parameters. We thus show how this leads to significant differences in the computed curves of the absorption cross-section of pure carbonaceous nanoparticles as a function of the frequency, with respect to calculations performed using parameters issued from graphite.

Michel Rérat
Université de Pau et des Pays de l'Adour, CNRS ,IPREM, E2S UPPA, Pau, France

Jean-Claude Rayez
Institut des Sciences Moléculaires, UMR CNRS 5255, Université de Bordeaux, France

Michel Devel (E-mail: michel.devel@femto-st.fr)
Institut FEMTO-ST UMR CNRS 6274 , Université Bourgogne Franche-Comté, Besançon, France

Balázs Fabián
Institut UTINAM - UMR CNRS 6213, Université Bourgogne Franche-Comté, Besançon, France (present address : Max Planck Institute of Biophysics, Theoretical Biophyics Department, 60438 Frankfurt am Main)

Sylvain Picaud (E-mail: sylvain.picaud@univ-fcomte.fr)
Institut UTINAM - UMR CNRS 6213, Université Bourgogne Franche-Comté, Besançon, France

1 Introduction

Combustion processes are responsible not only for gaseous emissions, among which CO_2, one of the main greenhouse gases, but also for particulate matter coming from uncomplete burning. This particulate matter comprises carbonaceous particles directly emitted by the combustion processes (combustion-generated particles) and, possibly, secondary organic aerosols (SOA) that are formed by the recombination of the emitted gases [1]. The formation of these SOA is more likely to occur in biomass fires or, for instance, when using biofuels as new sources of energy for transports [2]. Various nomenclatures exist to describe combustion-generated particles which are commonly referred as soot, black carbon (BC) or even brown carbon (BrC) depending on how these parti-

cles have evolved from their inception (or in other word, how mature they are) and how much they absorb light [3]. Note that elemental carbon (EC) is another term widely used in the aerosol community to describe particles that are extremely high in carbon relative to other elements, whereas the term organic carbon (OC) is used when these particles are composed of carbon combined with other atoms such as hydrogen or oxygen [3]. In addition, these nomenclatures can differ between combustion and atmospheric communities [3, 4]. Among emissions coming from combustion processes, carbonaceous particles (soot, BC, BrC) are known to be responsible for adverse health effects [5, 6] and are also suspected to contribute to climate warming [7]. Indeed, these carbonaceous particles may have both direct and indirect effects on the Earth's radiative balance [8]. Direct effect is related to the optical properties of the nanoparticles, i.e., their ability to absorb and scatter solar radiations [9], while indirect effect comes from their impact on cloud formation and properties by acting as more or less efficient cloud condensation nuclei [10, 11].

In contrast with CO_2 that may stay for tens of years in the atmosphere, combustion-generated particles are rather short-lived atmospheric compounds (about 4 to 10 years) so that every change in the use of, for instance, fossil energies, would lead to a fast change in the amount of carbonaceous particles in the atmosphere while the concentration of CO_2 will remain almost constant during a long period [12]. It is thus of the greatest importance to accurately know the radiative forcing related to carbonaceous particles, in particular to better constrain climate models that use data on the absorption and scattering properties of the various atmospheric constituents.

However, a quantification of the indirect effect of carbonaceous particles might remain challenging in the future due i) to the complexity of the corresponding phenomena involving their interaction with surrounding water to form cloud condensation nuclei and ii) to the various feedbacks of clouds on climate [13]. By contrast, a better characterization of the direct effect of combustion-generated particles on climate can be, in principle, expected because the process mainly depends on the determination of the optical properties of the nanoparticles themselves [14]. This would however require a better knowledge of the distributions of nanoparticle morphology and composition, from their inception to their growth and aging in the atmosphere [15, 16].

From a theoretical point of view, absorption and scattering properties can be computed on particles whose dielectric constant or refractive index is known. Thus, by assuming the shape, the size and even the internal composition (i.e., the EC/OC ratio) of the particles, macroscopic approaches such as the Lorenz-Mie theory and/or Rayleigh-Debye-Gans theory can reproduce quite well the measured optical properties of combustion-emitted particles [17, 18]. Moreover, powerful numerical approaches such as the T-matrix [19, 20] or the discrete dipole approximation (DDA) [21, 22] methods are now largely used for quantifying absorption and scattering of radiation by particles of arbitrary shape and by periodic structures. Nevertheless, the underlying assumptions of all these methods prevent taking into account all the atomistic details of the carbonaceous particles, such as the presence of numerous structural point defects at their surface [23], or the overlapping and necking phenomena observed when these particles form aggregates [24]. These features have been proven to have non negligible impact on the optical properties of the particles [25, 26, 27, 28] and, thus, they should not be ignored when aiming at a better quantification of the radiative forcing due to combustion-generated particles.

That is why we have recently developed a numerical method aiming at calculating optical properties of combustion-emitted nanoparticles that directly depend on their atomistic details.[29] This method, based on the point dipole interaction (PDI) model [30], has been proven well-suited for the calculations of the mass absorption coefficient of EC nanoparticles modeled at the atomic scale [27]. However, in this approach, not only the positions of the atoms but also their frequency-dependent polarizability have to be known, as input data. While the positions of the atoms can be inferred or modelled in a quite realistic way [25] from the results of more and more precise high-resolution electron microscopy studies [23], obtaining accurate values for the atomic frequency-dependent polarizability is far from being a trivial task. Indeed, up to now, using parameters optimized for graphite was unavoidable due to the lack of any reliable set of parameters especially tuned for carbon atoms in curved structures such as the onion-like particles evidenced in combustion emissions [31]. However, the polarizability values may likely change with the hybridization of the C atoms and it is now well established that combustion-emitted nanoparticles contain not only aromatic (sp^2) but also aliphatic (sp^3) carbons as well as carbon atoms with less than 3 neighbors at point-defect (vacancy) sites or at the edges of the nanocrystallites that constitute the surface or these nanoparticles [23, 28].

In the present paper, we focus on the C atoms that are imbedded in curved structures. We use an original reverse PDI-based method to calculate atomic frequency-dependent polarizability values for such C atoms, taking the C_{60} fullerene as a model system to fit our data. This method is based on the knowledge of the molecular frequency-dependent polarizabilities of this fullerene, calculated with the frequency-dependent coupled-perturbed method [32] as implemented in the code of quantum chemistry calculations CRYSTAL [33, 34]. We show that this high-level quantum chemistry approach represents an interesting alternative to the more often used Time Dependent Density Functional Theory (TD-DFT) [35], although it has never been previously used in this context. Then, the carbon atomic frequency-dependent

polarizability is deduced from a fitting procedure based on the reverse PDI-based method, in the frequency range in which the C_{60} molecular polarizability was calculated. This atomic frequency-dependent polarizability is finally used to recalculate the molecular polarizability of C_{60} with the original PDI-based method we developed few years ago [27, 29], for comparison with both the original quantum results and experimentally available data on these fullerene molecules. In addition, our original PDI-based method is also used to calculate the optical properties of model soot particles, based on the atomic frequency-dependent polarizability fitted in the present work, for comparison with previous results obtained using polarizability coming from graphite data.

The paper is organized as follows. Theoretical backgrounds and all the computational details on the ab-initio compution of the C_{60} molecular polarizability and subsequent parametrization of the carbon atomic polarizabilities are given in Sections 2 and 3, respectively. The corresponding results are detailed and discussed in Section 4, along with an application of the new parameters to representative nascent soot particles. Finally, the main conclusions of this study are summarized and future developments outlined in Section 5 .

2 Molecular polarizability calculation using CRYSTAL

2.1 Principle of the method

The static polarizability ($\overline{\overline{\alpha}}$) is a tensor of rank two, and its electronic contribution is defined as the derivative of the dipole moment (μ) of the clamped-ion system with respect to the field ($\mathbf{F}$):

$$\mu_i = \mu_i^0 + \sum_j \alpha_{ij} F_j + \cdots \tag{1}$$

where μ_i^0 and F_j are the components of the permanent dipole moment and of the field, respectively [36].

Electric properties of the free fullerene molecule are calculated as the derivatives of the dipole moment of the finite system with respect to the external field components. The external field induces dipole moments at the surface of the sphere creating an additive field inside it and decreasing the polarizability. This surface effect does not exist in the bulk of the fullerene crystal, and the polarizability of a unit cell is defined as the derivative of its dipole moment with respect to the mean field, or macroscopic field felt by the cell. It is worth noting that the macroscopic field is not the local field felt by each atom of the C_{60} sphere or at its center. In this periodic system for which the density of matter is defined as the inverse of the unit cell volume, the dielectric ε_{uv}-component of the bulk is related to the polarizability as follows:

$$\varepsilon_{uv} = \delta_{uv} + 4\pi\alpha_{uv}/V \tag{2}$$

where α_{uv} is the polarizability component of a unit cell in the bulk, and V its volume (see pages 404 and 409 in Ref. [37]). δ is the usual Kronecker symbol.

However, the dipole moment μ is ill-defined in the bulk, and the unbound electron position operator associated with the field perturbation for finite system cannot be used anymore. Nevertheless, it can be shown that its expression becomes equal to $\Omega = \mathbf{r} + \imath\nabla_{\mathbf{k}}$ in the Born Von Karman crystalline orbital (CO) basis set depending on $\mathbf{k}$-points of the reciprocal space, if the wavelength of the field is large with respect to the size of the unit cell [38, 39] as in the UV-visible spectroscopy, and keeping the hamiltonian block-diagonal at the first order of perturbation in this reciprocal space.

For (ω) frequency-dependent field, the second-order of perturbation response property in the independent-particles model described by occupied ($i_{\mathbf{k}}$) and virtual ($j_{\mathbf{k}}$) COs per $\mathbf{k}$-point is a complex function which can be described as the following sum over states expression for the diagonal component:

$$\alpha_{uu}(\omega) = \sum_{\mathbf{k}} \sum_{i}^{occ} \sum_{j}^{virt} f_{u,ij,\mathbf{k}} \frac{\left((\varepsilon_{j,\mathbf{k}} - \varepsilon_{i,\mathbf{k}})^2 - \omega^2\right) + \imath\eta\omega}{(\varepsilon_{j,\mathbf{k}} - \varepsilon_{i,\mathbf{k}})^2 - \omega^2)^2 + \eta^2\omega^2} \tag{3}$$

where $f_{u,ij,\mathbf{k}} = 2(\varepsilon_{j,\mathbf{k}} - \varepsilon_{i,\mathbf{k}})\langle i_{\mathbf{k}}|\Omega_u|j_{\mathbf{k}}\rangle^2$ is the oscilator strength between the $i_{\mathbf{k}}$ and $j_{\mathbf{k}}$ eigenvectors of the unperturbed Hartree-Fock, density functional theory (DFT) or hybrid hamiltonian with $\varepsilon_{i,\mathbf{k}}$ and $\varepsilon_{j,\mathbf{k}}$ eigenvalue, respectively, and η is a damping factor representing the inverse of time of life of excited states, and generally set to the resolution of experimental equipment ($\simeq 0.1$ eV in the UV-visible spectroscopy).

In Eq. 3, the orbital relaxation due to the electric field is not taken into account in the determination of the poles, $\omega_{ij,\mathbf{k}} = \varepsilon_{j,\mathbf{k}} - \varepsilon_{i,\mathbf{k}}$, and corresponding oscillator strengths, $f_{u,ij,\mathbf{k}}$, at resonance. The exciton effect correction can be included in following the frequency-dependent coupled-perturbed Hartree-Fock (CPHF) method of Karna and Dupuis [40]: the orbital relaxation is described by the derivative of the electron density with respect to the electric field involved in the bielectronic repulsion of the Fock operator which depends itself on this latter one. The iterative process is repeated till convergence of α_{uu} which depends on the orbital relaxation, starting from the sum over states (SOS) polarizability component value (Eq. 3). At convergence, the expression of the polarizability can be written as follows:

$$\alpha_{uu}(\omega) = \sum_{\mathbf{k}} \sum_{i}^{occ} \sum_{j}^{virt} \tilde{f}_{u,ij,\mathbf{k}} \frac{(\tilde{\omega}_{ij,\mathbf{k}}^2 - \omega^2) + \imath\eta\omega}{(\tilde{\omega}_{ij,\mathbf{k}}^2 - \omega^2)^2 + \eta^2\omega^2} \tag{4}$$

with new ($\tilde{f}_{u,ij,\mathbf{k}}$,$\tilde{\omega}_{ij,\mathbf{k}}$) couples of oscillator strengths and poles of the UV-visible spectrum [32]. Starting from pure DFT PBE [41] unrelaxed orbitals, the iterative self-consistent coupled-perturbed (CP) process shifts slightly the gap towards larger energy and the shape of the UV-visible absorption spectrum is not dramatically changed with respect to the SOS one. It is not the same with Hartree-Fock for which the

optical gap can be much smaller that the vertical (SOS) gap due to the exciton shift correction, while hybrid hamiltonian with a percentage of Hartree-Fock exchange can provide the same gap at the SOS and CP levels of calculation.

If the real part of the polarizability provides information on the refractive index dispersion ($n = \sqrt{\varepsilon}$ with ε related to α via Eq. 2) before first resonances, its imaginary part provides oscillator strengths at the pole resonances in the UV-visible absorption spectrum. The latter one can then be compared to experiment, at least near the optical gap. Both real and imaginary parts of ε can also be used to calculate the reflectivity and valence electron energy loss spectrum (VEELS). Comparison with experiment, when available, allows to validate the plotting of the molecular polarizability with respect to ω needed in the fits of atomic polarizabilities and then, in the determination of cross section for large organic molecules and soots.

2.2 Computational Details

2.2.1 Geometry and electronic structures

The structure of the molecule of fullerene has been built from a folded surface of graphene in the Ih icosahedron symmetry using the CRYSTAL program [33, 34] while the cell parameters and fractional coordinates of the three independent carbon atoms in the $Fm\bar{3}$ cubic crystal of fullerene (4 molecules per crystallographic cell) have been reoptimized from the crystalline structure given by Dorset and McCourt [42] and that can be found in the Crystalline Open Database website. Calculations have been performed with the pure DFT PBE functional [41] and an all-electron triple zeta valence plus polarization basis set of Gaussian-type functions has been adopted for the carbon atom (POB-TZVP [43]). The exponents of the outermost s, p and d shells are equal to 0.1644, 0.2674 and 0.8792 bohr^{-2}, respectively. The truncation criteria of the overlap, Coulomb and exchange infinite lattice series are controlled by five thresholds, T_i, which have been set to 7 (T_1-T_4) and 14 (T_5) (see the manual of CRYSTAL [34] for more details). The convergence threshold on energy for the self-consistent-field (SCF) procedure has been set to 10^{-8} hartree for structural optimizations calculation.

The DFT exchange-correlation contribution and its gradient are evaluated by numerical integration over the unit cell volume. The generation of the integration grid points is based on an atomic partition method, originally proposed by Becke [44]. Radial and angular points for the integration grid are generated through the Gauss-Legendre radial quadrature and Lebedev two-dimensional angular point distributions. The choice of a suitable grid is crucial both for numerical accuracy and costs. In this study the standard XLGRID pruned grid [34] with 75 radial and 434 angular points has been used, whose accuracy can be measured by comparing the integrated charge density of the C_{60} fullerene, 359.999766 electrons with the number of electrons in the unit cell (360).

In the periodic case, crystalline orbitals are combinations of Bloch functions built in the reciprocal space with **k**-points satisfying Born Von Karman conditions. The number of **k**-points is defined by the S-shrinking factor set to 4 and leading to 8 vectors in the irreducible Brillouin zone.

2.2.2 Molecular and crystal polarizabilities

The static polarizability of periodic systems has then been obtained from the coupled-perturbed Kohn-Sham (CPKS) method implemented in the CRYSTAL code (see refs. 45, 46, 47), and the CP iterative process, using PBE, was considered as converging when the variation of each independent diagonal polarizability component was less than 10^{-4} bohr^3 in absolute values from an iteration to the other. For both the spherical C_{60} molecule and cubic molecular crystal, there is only one independent component of the polarizabity. The static value is reported in Table 1. The molecular crystal is more stable than the free molecule, and the gap is smaller than the transition energy between the highest-occupied (HOMO) and lowest-unoccupied (LUMO) molecular orbitals, which leads to a larger polarizability in the bulk. The orbital relaxation taken into account in the CP calculation decreases the value of the polarizability by a factor 4 (SOS: 1811 bohr^3 to CP: 459 bohr^3) in the molecule due to important polarization effect at the surface of the fullerene sphere. Following the demonstration of Benedict et al. [48], the ratio between the relaxed and unrelaxed orbital polarizabilities is equal to:

$$\frac{\alpha^{CP}}{\alpha^{SOS}} = \frac{1}{1 + \alpha^{SOS}/R^3} \tag{5}$$

where R is the mean electronic sphere radius. Values of 1811 and 459 bohr^3 lead to $R = 4.5$ Å, which is a bit smaller than the van der Waals radius of the C_{60} molecule ($\simeq 5.5$ Å, ref. [49]) but larger than half its nucleus to nucleus diameter ($\simeq 3.5$ Å). This effect is much less (by a factor of 1.6) in the bulk.

On the other hand, the pure DFT PBE hamiltonian is known to underestimate the gap (1.08 eV compared to the experimental 2.15 eV value), and then to overestimate the static dielectric constant (4.74 instead of 4.0).

The dynamic polarizability can then be calculated with the frequency-dependent coupled-perturbed method implemented in CRYSTAL (see ref. [32]), providing the UV-visible absorption spectrum, reflectivity and VEELS from its real and imaginary parts obtained by scanning the field frequency.

Table 1 Conventional cell parameter (a in Å) of the Fm$\bar{3}$ space group (four molecules per cubic cell), energy of the unit cell (E) with respect to the free molecule and gap (in eV), static α^{SOS} and α^{CP} polarizability values (in bohr^3) of the free C_{60} molecule and primitive unit cell of the crystal. In parentheses, the dielectric constant.

	a	E	gap	α^{SOS}	α^{CP}
molecule	∞	0	1.76	1811	459
crystal	13.9	-1.46	1.08	2214 (7.09)	1359 (4.74)
exp.	14.3$^{(1)}$		2.15$^{(2)}$		(4.0)$^{(2)}$

(1): ref. [42]
(2): ref. [50]

3 PDI and Reverse PDI methods

3.1 PDI method

In our PDI-like approach [29], the dynamical polarizability tensor $\overline{\overline{\alpha}}(\omega)$ of a carbonaceous nanoparticle containing N carbon atoms is deduced from the knowledge of the atomic positions $\vec{r}_i$ and polarizability tensors $\overline{\overline{\alpha}}_i(\omega)$, following equalities :

$$\begin{aligned}\vec{p}(\omega) &= \overline{\overline{\alpha}}(\omega)\vec{E}_0(\omega) = \textstyle\sum_{i=1}^{N} \vec{p}_i(\omega) \\ &= \textstyle\sum_{i=1}^{N} \overline{\overline{\alpha}}_i(\omega)\vec{E}_{loc}(\vec{r}_i,\omega)\end{aligned} \tag{6}$$

where $\vec{p}$ is the total electrical dipole moment of the carbonaceous nanoparticle and $\vec{E}_0(\omega)$ is an external electric field applied to this nanoparticle. $\vec{p}_i$ is the dipole induced on atom i by the local electric field at its location $\vec{E}_{loc}(\vec{r}_i,\omega)$. This local field is written as the sum of the external field $\vec{E}_0(\omega)$ and of the electric field created at the position $\vec{r}_i$ by the dipoles induced on the other carbon atoms. Hence, the individual dipoles can be computed by solving the following linear system of equations [30]:

$\forall\, i = 1,...,N$

$$\vec{p}_i(\omega) = \overline{\overline{\alpha}}_i(\omega)\vec{E}_0(\omega) + \sum_{j=1}^{N} \overline{\overline{\alpha}}_i(\omega)\overline{\overline{T}}(\vec{r}_i,\vec{r}_j,\omega)\vec{p}_j(\omega) \tag{7}$$

where $\overline{\overline{T}}(\vec{r}_i,\vec{r}_j \neq i,\omega)$ can be computed with the double gradient of the generalized Green's function for the Helmholtz equation:

$$\overline{\overline{T}}(\vec{r}_i,\vec{r}_j \neq i,\omega) = -\frac{1}{\varepsilon_0}\left(\vec{\nabla}_{\vec{r}_i} \otimes \vec{\nabla}_{\vec{r}_j} + \frac{\omega^2}{c^2}\bar{\bar{I}}\right)\left(-\frac{e^{i\frac{\omega}{c}\left|\vec{r}_i-\vec{r}_j\right|}}{4\pi\left|\vec{r}_i-\vec{r}_j\right|}\right) \tag{8}$$

with c the speed of light and ε_0 the permittivity of vacuum.

Because in PDI the point dipoles are supposed to represent atoms much smaller than the discretization volumes used in the discrete-dipole approximation method (DDA)[51], the $i = j$ terms of the interaction tensor $\overline{\overline{T}}$ are assumed to simplify to:

$$\overline{\overline{T}}(\vec{r}_i,\vec{r}_i,\omega) = i\frac{2}{3}\frac{\omega^3}{c^3}\frac{1}{4\pi\varepsilon_0} \tag{9}$$

Equation (7) can then be written as a $3N \times 3N$ matrix system whose resolution gives a $3 \times 3N$ vector containing the dipoles $\vec{p}_i(\omega)$ on each carbon atom, corresponding to three values of $\vec{E}_0$ successively along the three coordinates axes. Once the values of the dipoles are self-consistently computed by the above procedure, they can be used to compute various optical quantities of interest (such as the Müller matrix or the extinction, diffusion and absorption cross-sections) as in the DDA method [51].

3.2 Reverse PDI method

As shown by the equations above, the calculation of the molecular polarizability tensor $\overline{\overline{\alpha}}(\omega)$ requires the knowledge of the atomic anisotropic tensors $\overline{\overline{\alpha}}_i(\omega)$. Thus, in previous studies [27, 29], we made use of the graphite dielectric constants tabulated by Draine [52, 53] and the generalized Clausius–Mossotti relation proposed by Senet et al. [54] and confirmed by Andersen and Bonderup [55] to compute anisotropic carbon atomic polarizabilities and, then, we calculated the molecular polarizability tensor of various carbonaceous nanoparticles modeling nascent soot. In the present approach, we directly calculate the isotropic atomic carbon polarizability that allows the best fit of the C_{60} polarizability tensor $\overline{\overline{\alpha}}_{C_{60}}(\omega)$ computed with CRYSTAL. In other words, rather than knowing the atomic polarizability to derive the molecular polarizability with the PDI-like approach, we use a reverse method to find the isotropic atomic polarizability $\alpha_C(\omega)$ that gives the best fit of the molecular polarizability tensor $\overline{\overline{\alpha}}_{C_{60}}(\omega)$ with respect to the quantum values. The fitting procedure is initialized using $\alpha_C(\omega) = (2\alpha_{C,\perp}(\omega) + \alpha_{C,\parallel}(\omega))/3$ with $\alpha_{C,\perp}$ and $\alpha_{C,\parallel}$ our previous anisotropic carbon polarizabilities derived from Draine's [52, 53] graphite parameterization ($\perp$ and $\parallel$ meaning respectively perpendicular and parallel to the c axis of graphite).

4 Results

4.1 DFT results for the dielectric permittivity of C_{60}

First, to check the accuracy of our quantum approach, we used the dynamic polarizability of a unit cell calculated with the CRYSTAL code and deduced from Eq. 2, the dielectric constant of the C_{60} cubic crystal which can be, for instance, directly compared to data from Electron Energy Loss Spectroscopy (EELS) experiments. Notice that the theoretical

calculations have been performed frequency by frequency, with a damping term, $\eta\omega$ (see Eq. 4), that variates linearly with the frequency and makes smoother the peak height as the frequency increases. Of course, the corresponding resolution of the theoretical results (i.e., the number of frequency values considered and the damping factor used) relies on a compromise between numerical efficiency (duration of the calculations) and minimum number of points that is necessary to ensure the validity of the fitting procedure used further, in the reverse PDI-based method (see below).

Plots of the real and imaginary parts of the dielectric constant of the C_{60} cubic crystal, as well as the corresponding electron loss function (ELF) ($\mathrm{Im}[-1/\varepsilon(\omega)]$), as computed with CRYSTAL at SOS and CP levels, are thus reported in Figures 1 and 2, respectively, together with the experimental data coming from EELS studies of Sohmen et al. [50]. The experimental resolution is equal to 0.14 eV [50].

As it can be seen on Figure 2, the theoretical results are in fair agreement with the experimental ones, especially below 10 eV. In this low-energy region of the spectrum, the large peak around 6 eV, corresponding to the collective excitations of the $2p_z$ electron subsystem in sp^2 carbon (the so-called π plasmon), is indeed well represented in the theoretical results, as well as the resonances related to excitations from π to $\pi^\star$ orbitals below 5 eV. Note that such resonances are typical of fullerenic crystals and they are not observed in graphite for instance, due to symmetry consideration [56]. In addition, in this low-energy range of the spectrum, theoretical results obtained at the SOS level appear slightly too red-shifted when compared to the experimental data, in contrast with results obtained at the CP level that thus appear quite better.

The situation is somewhat more complicated above 10 eV. In this energy range, many resonances are calculated at both SOS and CP levels, that can be more or less related with those observed in the experimental spectrum and due to, for instance, the collective motions of all 2s and 2p electrons (the so-called σ plasmons, around 18 eV) and to $\sigma+\pi$ plasmons around 27 eV [50, 57]. In this high-energy range, the results obtained at SOS level seems to be slightly better than those obtained at the CP level, at least when looking at the peak positions with respect to the experimental values.

Overall, the comparison with the experimental data validates the results of the quantum calculations performed with the CRYSTAL code, especially below 10 eV, i.e., in the UV-Visible region of the spectra which is of interest when dealing with absorption properties of carbonaceous systems in relation with their influence on the global climate warming.

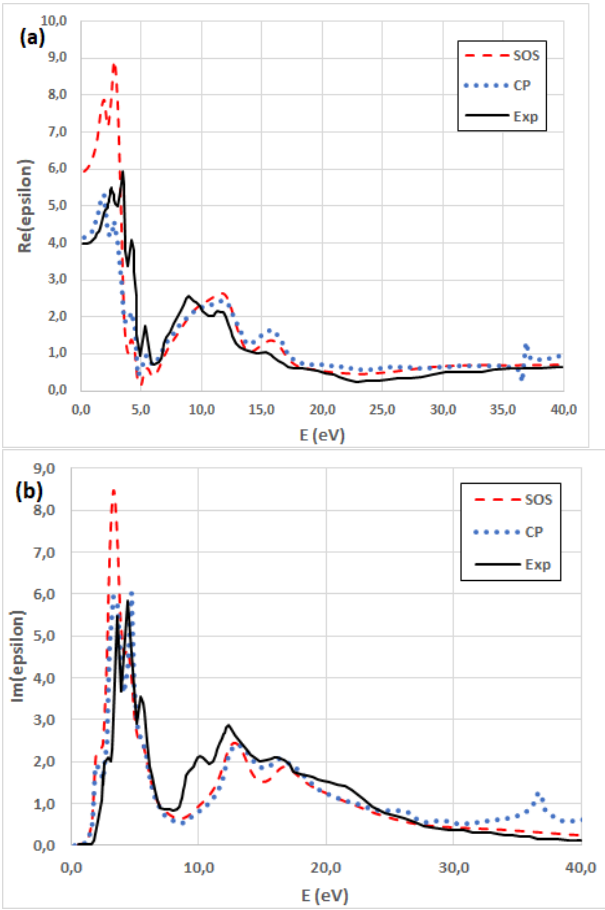

Fig. 1 Real (a) and imaginary (b) parts of the dielectric constant of the C_{60} crystal at the SOS (red dashed curve) and CP (blue dotted curve) levels of calculation in CRYSTAL. Experimental results [50] are also indicated (black solid line curve) for comparison.

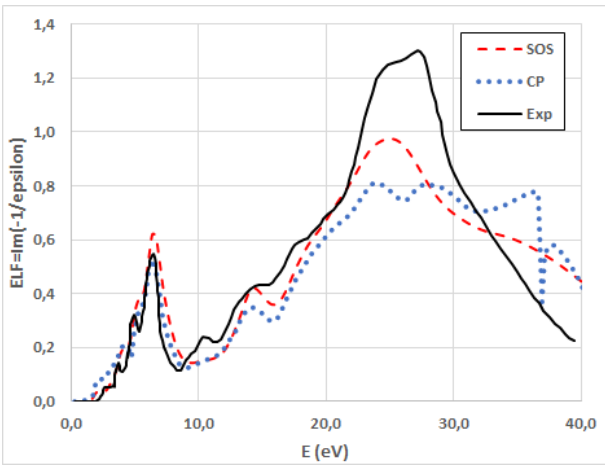

Fig. 2 Electron loss function of the C_{60} crystal at the SOS (red dashed curve) and CP (blue dotted curve) levels of calculation in CRYSTAL. Experimental results [50] are also indicated (black solid line curve) for comparison.

4.2 Carbon isotropic polarizabilities from the reverse PDI procedure

The molecular frequency-dependent polarizability values calculated at the quantum level in CRYSTAL have been used to fit the atomic frequency-dependent polarizability of C atoms in C_{60}, by using the reverse PDI method presented above. The real and imaginary parts of the corresponding atomic frequency-dependent isotropic polarizability of C atoms are given in Fig.3. The results of our calculations are compared with the two components of our previous anisotropic carbon polarizability tensors derived from Draine's graphite parameterization,[52, 53] that have served to initialize the fitting procedure. It is clearly shown that the curve issued from the present approach is much more similar to the component of the anisotropic polarizability parallel to the local carbon plane than to the component perpendicular to this local plane. Furthermore, the hybridization of the σ and π molecular orbitals due to the curvature of the local carbon sheet in C_{60} results in finer sub-structures.

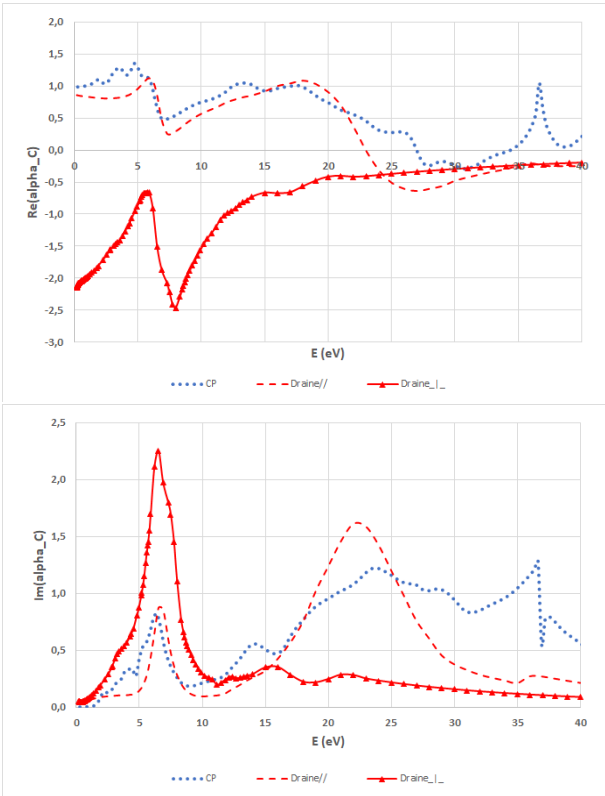

Fig. 3 Real (a) and imaginary (b) parts of the atomic polarizability of C atoms in C_{60} (divided by $4\pi\varepsilon_0$), as computed from the reverse PDI-based method applied to the molecular polarizabiliy of C_{60} calculated with CRYSTAL at the CP level (blue dotted curve); as computed from the component parallel to the local carbon plane of the anisotropic carbon polarizabilities derived from Draine's parameterization for the permittivity of graphite (red dashed curve) ; as computed from the component perpendicular to the local carbon plane of the anisotropic carbon polarizabilities derived from Draine's parameterization for the permittivity of graphite (red curve and triangular symbols).

4.3 Photoabsorption cross-sections from PDI with C polarizabilities from reverse PDI

The original PDI-based method [29] has been applied to calculate the photoabsorption cross-section of C_{60}, from the newly estimated frequency-dependent polarizability of the carbon atoms. The corresponding calculated photoabsorption cross-section is given in Figure 4, together with available experimental data coming from studies of graphite[52] and C_{60} crystal[50], for comparison. Notice that the curves in this figure basically exhibit the same features as in Figure 2, because the photoabsorption cross section is directly related to the electron loss function. However, it is important to recall that whereas Figure 2 comes directly from the CRYSTAL calculations, the photoabsorption cross section shown in Figure 4 is derived from carbon atomic polarizabilities through the PDI-based method. In other words, this figure is a benchmark for our determination of the atomic polarizability of C atoms in C_{60}.

As it can be seen, the theoretical results are in fair agreement with the experimental ones, especially below 10 eV where the π plasmon and the $\pi \rightarrow \pi^{\star}$ resonances are well represented. By contrast, when the carbon atomic polarizabilities are derived from graphite data, they do not account for these resonances, which confirms that data coming from flat sp^2 systems cannot properly represent absorption properties of curved carbonaceous systems. The overall agreement between the theoretical results and those coming from experimental measurements remains quite good at higher energies (above 10 eV) although, as stated above, the number of resonances obtained in the theoretical approach is questionable with respect to the observations. Nevertheless, in optical regions of interest for atmospheric and interstellar sciences, the presently determined atomic polarizability values for C atoms together with using the PDI-based method, represent an interesting alternative to the usual other approaches such as DDA.

In addition, our original PDI-based method has also been used to calculate the mass specific photoabsorption cross section (MAC) coefficients (defined as the ratio of the photoabsorption cross section to the total mass of the nanostructure) of model soot particles of nanometer size, on the basis of the atomic frequency-dependent polarizability fitted in the present work from the CRYSTAL results. For comparison, similar calculations have also been performed with carbon atomic polarizabilities determined by using the reverse PDI method with the molecular polarizabiliy of C_{60} calculated from the EELS data of Sohmen et al.[50] and the generalized Clausius-Mossotti formula of Senet at al.[54]. An additional comparison has also been made using anisotropic carbon

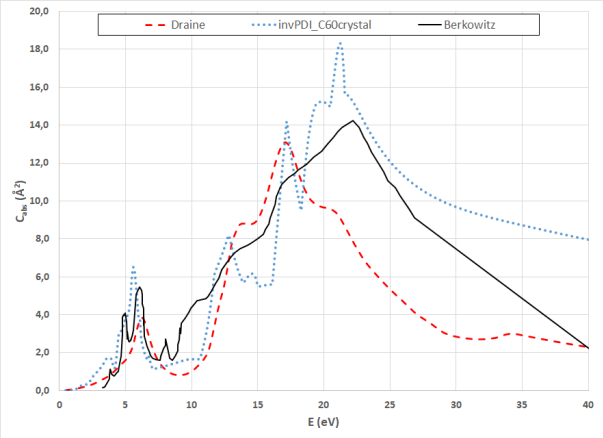

Fig. 4 Photoabsorption cross section (C_{abs}) of a C_{60} molecule as a function of the energy of the incident radiation. The red, dashed curve, shows the results computed from the frequency-dependent anisotropic carbon atomic polarizability using Draine's parameterization for graphite and the Lorentz factors computed by Senet et al.[54], whereas the blue, dotted curve, gives the values computed using the frequency-dependent carbon atomic polarizability obtained from the reverse PDI-based method using a fit of the molecular polarizabiliy of C_{60} calculated with CRYSTAL. The experimental data compiled by Berkowitz [58] are represented as a black solid curve.

atomic polarizabilities coming from graphite,[53] as in our previous work.[27]

Various nanoparticles have been considered for these calculations, their atomistic structure being based on the structure of four-shell fullerene onions, in which first a given number of carbon atoms has been randomly removed, followed by a full relaxation process achieved through molecular dynamics simulations in which the adaptative intermolecular reactive empirical bond order (AIREBO) potential model[59] has been used to represent the carbon–carbon interactions. Thus, two small (labeled S_{2133} and S_{2207}) and two big (S_{3774} and S_{4198}) soot nanoparticles have been built by removing either 1033 or 1107 atoms from the C240@C540@C960@C1500 fullerene onion, and either 962 or 1386 atoms from the C540@C960@C1500@C2160 onion, respectively.[25, 27, 29]

The curves given in Fig. 5 show that the MAC calculated using the CRYSTAL-based polarizabilities in the PDI approach agree fairly well with those obtained with the polarizabilities based on the experimental data of Sohmen et al.[50] By contrast, these results significantly differ from those obtained when using polarizabilities coming from graphite data,[53, 27] which exhibit much less resonances, especially in the [200-400] nm range and which also converge to smaller MAC values at long wavelengths, with the exception of the S_{2207} soot nanoparticle. However, it is worth noting that the results of the different approaches vary quite significantly from one soot nanoparticle to another one, showing thus not only the strong influence of the polarizability values, but also of the atomic positions on the MAC calculations. Thus, the

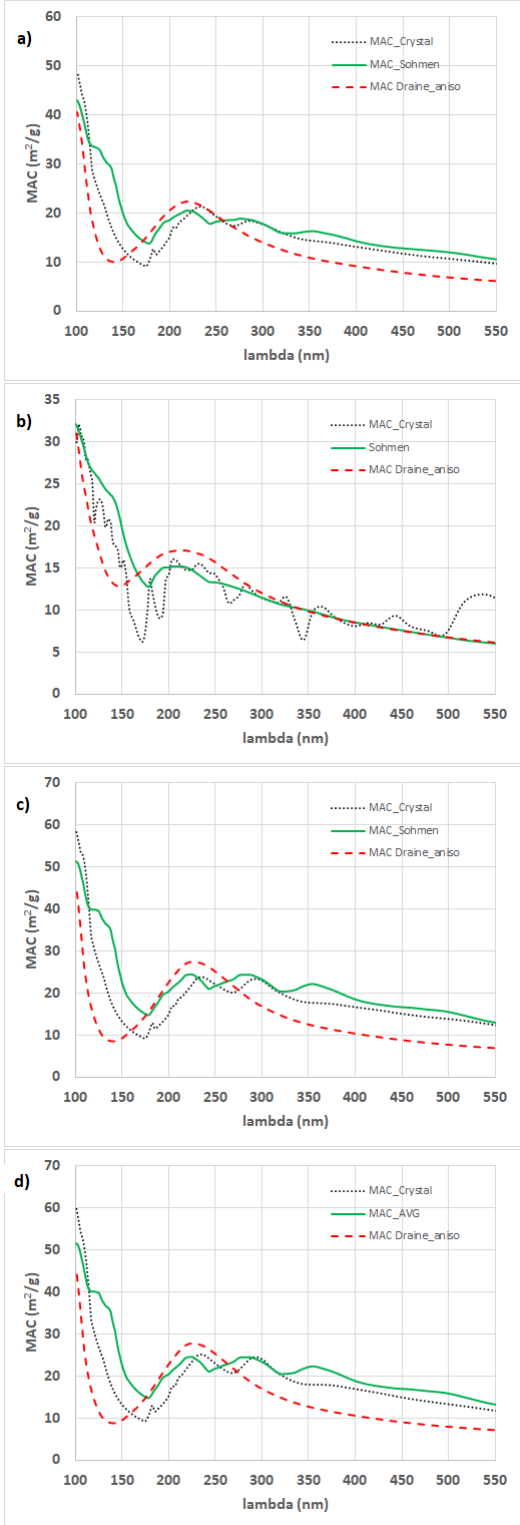

Fig. 5 Mass Absorption Cross-section (MAC in $m^2 \cdot g^{-1}$) of small soot nanoparticles made of (a) 2133, (b) 2207, (c) 3774, and (d) 4198 carbon atoms, as computed from the PDI method, using the isotropic atomic polarizabilities fitted here from the molecular polarizabiliy of C_{60} calculated with CRYSTAL (black dotted curves) or computed from EELS data[50] with the Lorentz factors computed by Senet et al.[54] (green solid curves). Red dashed curves represent the results for similar calculations performed when using carbon atomic anisotropic polarizabilities derived from graphite data.[53, 27]

similarities between the MAC curves obtained for the S_{2207} soot nanoparticle when using three different parametrizations of the C atomic polarisabilities including that coming from graphite, could appear as being rather fortuitous.

Unfortunately, as far as we know, experimental measurements of the MAC of individual carbonaceous nanoparticles are not available yet, and it is thus difficult to assess the real accuracy of the present calculations. However, our results clearly show that optical properties of soot nanoparticles, calculated using parameters derived from curved carbonaceous structures may significantly differ from those based on the planar graphite surface.

5 Conclusion

Here, we have used, for the first time, the code of quantum chemistry calculations CRYSTAL to compute the frequency-dependent polarizability of the C_{60} fullerene, either isolated or in a crystal. Then, we have deduced the corresponding atomic frequency-dependent polarizability of C atoms pertaining to curved structures, by using an original fitting procedure called the reverse PDI-based method. We have shown that the corresponding results are able to represent fairly well the experimentally measured absorption-cross section of C_{60}, in contrast to the previously used atomic polarizability values based on graphite data. More specifically, the resonances observed below 10 eV are well represented by the present theoretical data only, indicating that parameters coming from graphite measurements cannot be suitable to accurately represent sp^2 carbon atoms involved in curved structures. A similar conclusion has been reached when considering the calculations of the MAC of model soot nanoparticles.

We thus believe that the values of the carbon atomic polarizability determined here can actually serve for the determination of the optical properties of carbonaceous structures of atmospheric or interstellar interest such fullerenes and their derivatives, as well as soot or small carbonaceous grains, on the basis of their atomistic details, through the PDI method[27, 29]. This would represent a nice, and hopefully more precise, alternative to the usual DDA or T-matrix approaches which usually neglect those levels of description.

However, it is worth mentioning that because real soot nanoparticles are made of carbon nanocrystallites,[23] they do not only contain sp^2, aromatic, carbon atoms, but also defects such as atomic vacancies, and carbon atoms located at the nanocrystallite edges[23]. In addition, mature soot may contain many aliphatic carbons, together with other atoms such as H and O, that likely come from organic coating.[60] These various constituents of soot are known to impact their light absorption and scattering[16, 61] and, as a consequence, the optical properties of soot should be calculated using the frequency-dependent polarizablities of all these atoms.

These data might be determined by reverse PDI-based calculations such as those presented here, by using for the fits of the atomic polarizabilities a set of molecular polarizabilities calculated at the quantum level for organic molecules containing various chemical functions, such as alcohols or carboxylic acids. This work is currently in progress.

Acknowledgments

This work has been done in the framework of the GDR CNRS 3622 (GDR SUIE) which is acknowledged for financial support. We would like to acknowledge the Direction du Numérique de l'Université de Pau et des Pays de l'Adour for the computing facilities provided when using the CRYSTAL code. The calculations related to the reverse PDI and PDI methods have been performed on the supercomputer facilities of the Mésocentre de calcul de Franche-Comté which is gratefully acknowledged.

References

1. A Limbeck, M Kulmala, and H Puxbaum. Secondary organic aerosol formation in the atmosphere via heterogeneous reaction of gaseous isoprene on acidic particles. *Geophys Res Lett*, 30(19): 1996, 2003.
2. G Stefenelli, J Jiang, A Bertrand, E Bruns, S Pieber, U Baltensperger, N Marchand, S Aksoyoglu, A Prévôt, J Slowik, and I El Haddad. Secondary organic aerosol formation from smoldering and flaming combustion of biomass: a box model parametrization based on volatility basis set. *Atmos Chem Phys*, 19:11461–11484, 2019.
3. H Michelsen, M Colket, P-E Bengtsson, A D'anna, P Desgroux, B Haynes, J Miller, G Nathan, H Pitsch, and H Wang. A review of terminology used to describe soot formation and evolution under combustion and pyrolytic conditions. *ACS Nano*, 14:12470–12490, 2020.
4. P Buseck, K Adachi, A Gelencsér, É Tompa, and M Pósfai. Are black carbon and soot the same? *Atmos Chem Phys Discuss*, 12: 24821–24846, 2012.
5. NAH Janssen, G Hoek, M Simic-Lawson, P Fischer, L Van Bree, H ten Brink, M Keuken, R Atkinson, R Anderson, B Brunekreef, and FR Cassee. Black carbon as an additional indicator of the adverse health effects of airborne particles compared with PM_{10} and $PM_{2.5}$. *Environ Health Perspect*, 119:1691–1699, 2011.
6. Y Li, D Henze, D Jack, B Henderson, and P Kinney. Assessing public health burden associated with exposure to ambient black carbon in the united states. *Sci Total Environ*, 539:515–525, 2015.
7. T Stocker, D Qin, G Plattner, M Tignor, S Allen, J Boschung, A Nauels, Y Xia, V Bex, and P Midgley. Climate change 1995: The science of climate change. contribution of working group I to the second assessment report of the intergovernmental panel on climate change. *Global Environl Change*, 7(2):186–187, 2013.
8. V Ramanathan and G Carmichael. Global and regional climate changes due to black carbon. *Nature Geoscience*, 1(4):221–227, 2008.
9. T Bond and R Bergstrom. Light absorption by carbonaceous particles: An investigative review. *Aerosol Sci Tech*, 40(1):27–67, 2006.
10. M Jacobson. Effects of externally-through-internally-mixed soot inclusions within clouds and precipitation on global climate. *The Journal of Physical Chemistry A*, 110(21):6860–6873, 2006.

11. L Qi, Q Li, C He, X Wang, and J Huang. Effects of wegener-bergeron-findeisen process on global black carbon distribution. *Atmos Chem Phys*, 17:7459–7479, 2017.
12. T Bond, S Doherty, D Fahey, P Forster, T Berntsen, B Deangelo, M Flanner, S Ghan, B Kärcher, D Koch, S Kinne, Y Kondo, P Quinn, M Sarofim, M Schultz, M Schulz, C Venkataraman, H Zhang, S Zhang, N Bellouin, S Guttikunda, P Hopke, M Jacobson, J Kaiser, Z Klimont, U Lohmann, J Schwarz, D Shindell, T Storelvmo, S Warren, and C Zender. Bounding the role of black carbon in the climate system: A scientific assessment. *J Geophy Res: Atmospheres*, 118(11):5380–5552, 2013.
13. G Stephens. Cloud feedbacks in the climate system: A critical review. *J Climate*, 18(2):237–273, 2005.
14. J Radney, R You, X Ma, J Conny, M Zachariah, J Hodges, and C Zangmeister. Dependence of soot optical properties on particle morphology: Measurements and model comparisons. *Environ Sci Technol*, 48(6):3169–3176, 2014.
15. G Kelesidis and S Pratsinis. Soot light absorption and refractive index during agglomeration and surface growth. *Proceedings of the Combustion Institute*, 37(1):1177–1184, 2019.
16. G Kelesidis, C Bruun, and S Pratsinis. The impact of organic carbon on soot light absorption. *Carbon*, 172:742–749, 2021.
17. J Kim, H Bauer, T Dobovičnik, R Hitzenberger, D Lottin, D Ferry, and A Petzold. Assessing optical properties and refractive index of combustion aerosol particles through combined experimental and modeling studies. *Aerosol Sci Technol*, 49(5):340–350, 2015.
18. C He. *Radiative properties of atmospheric black carbon (soot) particles with complex structures*, pages 219–254. Springer, 2019.
19. D Mackowski and M Mishchenko. Calculation of the T-matrix and the scattering matrix for ensembles of spheres. *J Opt Soc Am A*, 13 (11):2266, 1996.
20. M Mishchenko, L Travis, and D Mackowski. T-matrix computations of light scattering by nonspherical particles: A review. *JQSRT*, 55(5):535–575, 1996.
21. B Draine and P Flatau. Discrete-dipole approximation for scattering calculations. *J Opt Soc Am A*, 11(4):1491, 1994.
22. K Skorupski. Using the DDA (discrete dipole approximation) method in determining the extinction cross section of black carbon. *Metrol Meas Syst*, 22(1):153–164, 2015.
23. P Parent, C Laffon, I Marhaba, D Ferry, T Regier, I Ortega, B Chazallon, Y Carpentier, and C Focsa. Nanoscale characterization of aircraft soot: A high-resolution transmission electron microscopy, raman spectroscopy, X-ray photoelectron and near-edge X-ray absorption spectroscopy study. *Carbon*, 101:86–100, 2016.
24. C Oh and C Sorensen. The effect of overlap between monomers on the determination of fractal cluster morphology. *J Coll Int Sci*, 193(1):17–25, 1997.
25. G Hantal, S Picaud, P Hoang, V Voloshin, N Medvedev, and P Jedlovszky. Water adsorption isotherms on porous onionlike carbonaceous particles. simulations with the grand canonical monte carlo method. *J Chem Phys*, 133(14):144702, 2010.
26. K Skorupski and J Mroczka. Effect of the necking phenomenon on the optical properties of soot particles. *JQSRT*, 141:40–48, 2014.
27. C. García Fernández, S. Picaud, and M. Devel. Calculations of the mass absorption cross sections for carbonaceous nanoparticles modeling soot. *JQSRT*, 164:69–81, 2015.
28. A Bescond, J Yon, F-X Ouf, C Rozé, A Coppalle, P Parent, D Ferry, and C Laffon. Soot optical properties determined by analyzing extinction spectra in the visible near-UV: Toward an optical speciation according to constituents and structure. *J Aerosol Sci*, 101: 118–132, 2016.
29. F Moulin, M Devel, and S Picaud. Optical properties of soot nanoparticles. *JQSRT*, 109(10):1791–1801, 2008.
30. J Applequist, J Carl, and K-K Fung. Atom dipole interaction model for molecular polarizability. application to polyatomic molecules and determination of atom polarizabilities. *J Am Chem Soc*, 94(9): 2952–2960, 1972.
31. J Martin, K Bowal, A Menon, R Slavchov, J Akroyd, S Mosbach, and M Kraft. Polar curved polycyclic aromatic hydrocarbons in soot formation. *Proc Comb Inst*, 37(1):1117–1123, 2019.
32. A Ferrari, R Orlando, and M Rérat. Ab initio calculation of the ultraviolet–visible (UV-vis) absorption spectrum, electron-loss function, and reflectivity of solids. *J Chem Theor Comp*, 11(7):3245–3258, 2015.
33. R Dovesi, A Erba, R Orlando, C Zicovich-Wilson, B Civalleri, L Maschio, M Rérat, S Casassa, J Baima, S Salustro, and B Kirtman. Quantum-mechanical condensed matter simulations with CRYSTAL. *WIREs Comput Mol Sci*, 8(4):e1360, 2018.
34. R. Dovesi, V. Saunders, C. Roetti, R. Orlando, C. Zicovich-Wilson, F. Pasquale, B. Civalleri, K. Doll, N. M. Harrison, I. J. Bush, P. D'arco, M. Llunell, M. Causà, Y. Noël, L. Maschio, A. Erba, Rérat M., and S. Casassa. CRYSTAL17 User's Manual. University of Torino, 2017, Torino, Italy, 2017.
35. M Marques and E Gross. *Time-Dependent Density Functional Theory*, volume 55, pages 144–184. Springer Berlin Heidelberg, 2004.
36. A. D. Buckingham. Polarizability and hyperpolarizability. *Phil. Trans. R. Soc. Lond. A*, 293:239–248, 1979.
37. Kittel. *Introduction to Solid State Physics*. John Wiley, New York, 1976.
38. E. I. Blount. *Formalisms of Band Theory*, volume 13 of *Solid State Physics*, pages 305–373. Academic Press, New York, 1962.
39. P. Otto. Calculation of the polarizability and hyperpolarizabilities of periodic quasi-one-dimensional systems. *Phys Rev B*, 45(19): 10876–10885, 1992.
40. S Karna and M Dupuis. Frequency dependent nonlinear optical properties of molecules: Formulation and implementation in the hondo program. *J Comput Chem*, 12(4):487–504, 1991.
41. J Perdew, K Burke, and M Ernzerhof. Generalized Gradient Approximation made simple. *Phys Rev Lett*, 77(18):3865–3868, 1996.
42. DL Dorset and MP McCourt. Disorder and the molecular packing of C_{60} buckminsterfullerene: a direct electron-crystallographic analysis. *Acta Cryst A*, 50(3):344–351, 1994.
43. M Peintinger, D Oliveira, and T Bredow. Consistent gaussian basis sets of triple-zeta valence with polarization quality for solid-state calculations. *J Comput Chem*, 34(6):451–459, 2013.
44. A. Becke. A multicenter numerical integration scheme for polyatomic molecules. *J Chem Phys*, 88(4):2547–2553, 1988.
45. M Ferrero, M Rérat, R Orlando, and R Dovesi. The calculation of static polarizabilities of 1-3D periodic compounds. the implementation in the crystal code. *J Comput Chem*, 29(9):1450–1459, 2008.
46. M Ferrero, M Rérat, R Orlando, and R Dovesi. Coupled perturbed hartree-fock for periodic systems: The role of symmetry and related computational aspects. *J Chem Phys*, 128(1):014110, 2008.
47. R Orlando, V Lacivita, R Bast, and K Ruud. Calculation of the first static hyperpolarizability tensor of three-dimensional periodic compounds with a local basis set: A comparison of LDA, PBE, PBE0, B3LYP, and HF results. *J Chem Phys*, 132(24):244106, 2010.
48. L Benedict, S Louie, and M Cohen. Static polarizabilities of single-wall carbon nanotubes. *Phys Rev B*, 52(11):8541–8549, 1995.
49. R Qiao, A Roberts, A Mount, S Klaine, and P Ke. Translocation of C_{60} and its derivatives across a lipid bilayer. *Nano Lett*, 7(3): 614–619, 2007.
50. E. Sohmen, J. Fink, and W. Krätschmer. Electron energy-loss spectroscopy studies on C_{60} and C_{70} fullerite. *Zeit Phys B Cond Matt*, 86(1):87–92, 1992.
51. B Draine. The discrete-dipole approximation and its application to interstellar graphite grains. *Astrophys J*, 333:848, 1988.
52. B Draine and H Lee. Optical properties of interstellar graphite and silicate grains. *Astrophys J*, 285:89, 1984.

53. B Draine. Scattering by interstellar dust grains. II. X-rays. *Astrophys J*, 598(2):1026–1037, 2003.
54. P. Senet, L. Henrard, Ph. Lambin, A. Lucas, H. Kuzmany, J. Fink, M. Mehring, and S. Roth. A one parameter model of the UV spectra of carbon. In *Proceedings of the International Winterschool on Electronic Properties of Novel Materials. Progress in Fullerene Research*, pages 393–396. World Scientific, 1994.
55. J. Andersen and E. Bonderup. Local field corrections for light absorption by fullerenes. *European Phys J D*, 11(3):435–448, 2000.
56. S Saito and A Oshiyama. Cohesive mechanism and energy bands of solid C_{60}. *Phys Rev Lett*, 66(20):2637–2640, 1991.
57. A Lucas, L Henrard, and P Lambin. Plasmons on spherical carbon shells. *Nuclear Instr Meth Phys Res B*, 96(3-4):470–477, 1995.
58. J Berkowitz. Sum rules and the photoabsorption cross sections of C_{60}. *J Chem Phys*, 111(4):1446–1453, 1999.
59. S Stuart, A Tutein, and J Harrison. A reactive potential for hydrocarbons with intermolecular interactions. *J Chem Phys*, 112(14): 6472–6486, 2000.
60. J Yan, X Wang, P Gong, C Wang, and Z Cong. Review of brown carbon aerosols: Recent progress and perspectives. *Sci Total Environ*, 634:1475–1485, 2018.
61. G Lefevre, J Yon, M Bouvier, F Liu, and A Coppalle. Impact of organic coating on soot angular and spectral scattering properties. *Environ Sci Technol*, 53(11):6383–6391, 2019.